

Quasi-plastic deformation mechanisms and inverse Hall-Petch relationship in nanocrystalline boron carbide under compression

Zhen Yue(岳珍), Jun Li(李君), Lisheng Liu(刘立胜), and Hai Mei(梅海)
Citation: Chin. Phys. B, 2024, 33 (**8**): 086105. DOI: 10.1088/1674-1056/ad4989

What follows is a list of articles you may be interested in

Structural stability and ion migration of Li_2MnO_3 cathode material under high pressures

Ze-Ren Xie(谢泽仁), Si-Si Zhou(周思思), Bei-Bei He(贺贝贝), Huan-Wen Wang(王欢文), Yan-Sheng Gong(公衍生), Jun Jin(金俊), Xiang-Gong Zhang(张祥功), and Rui Wang(汪锐)
Chin. Phys. B, 2023, 32 (**12**): 126101. DOI: 10.1088/1674-1056/ace2b1

Prediction of superionic state in LiH_2 at conditions enroute to nuclear fusion

Fude Li(李福德), Hao Wang(王豪), Jinlong Li(李津龙), and Huayun Geng(耿华运)
Chin. Phys. B, 2023, 32 (**10**): 106103. DOI: 10.1088/1674-1056/acea68

Pressure-induced phase transition and electronic structure evolution in layered semimetal $HfTe_2$

Mei-Guang Zhang(张美光), Lei Chen(陈磊), Long Feng(冯龙), Huan-Huan Tuo(拓换换), Yun Zhang(张云), Qun Wei(魏群), and Pei-Fang Li(李培芳)
Chin. Phys. B, 2023, 32 (**8**): 086101. DOI: 10.1088/1674-1056/acd2bf

Equal compressibility structural phase transition of molybdenum at high pressure

Lun Xiong(熊伦), Bin Li(李斌), Fang Miao(苗芳), Qiang Li (李强), Guangping Chen(陈光平), Jinxia Zhu(竹锦霞), Yingchun Ding(丁迎春), and Duanwei He(贺端威)
Chin. Phys. B, 2022, 31 (**11**): 116102. DOI: 10.1088/1674-1056/ac673a

Structural evolution and bandgap modulation of layered β-$GeSe_2$ single crystal under high pressure

Hengli Xie(谢恒立), Jiaxiang Wang(王家祥), Lingrui Wang(王玲瑞), Yong Yan(闫勇), Juan Guo(郭娟), Qilong Gao(高其龙), Mingju Chao(晁明举), Erjun Liang(梁二军), and Xiao Ren(任霄)
Chin. Phys. B, 2022, 31 (**7**): 076101. DOI: 10.1088/1674-1056/ac6db8

Quasi-plastic deformation mechanisms and inverse Hall–Petch relationship in nanocrystalline boron carbide under compression

Zhen Yue(岳珍), Jun Li(李君)[†], Lisheng Liu(刘立胜)[‡], and Hai Mei(梅海)

Hubei Key Laboratory of Theory and Application of Advanced Materials Mechanics, Wuhan University of Technology, Wuhan 430070, *China*

(Received 21 December 2023; revised manuscript received 10 April 2024; accepted manuscript online 10 May 2024)

Grain boundaries (GBs) play a significant role in the deformation behaviors of nanocrystalline ceramics. Here, we investigate the compression behaviors of nanocrystalline boron carbide (nB_4C) with varying grain sizes using molecular dynamics simulations with a machine-learning force field. The results reveal quasi-plastic deformation mechanisms in nB_4C: GB sliding, intergranular amorphization and intragranular amorphization. GB sliding arises from the presence of soft GBs, leading to intergranular amorphization. Intragranular amorphization arises from the interaction between grains with unfavorable orientations and the softened amorphous GBs, and finally causes structural failure. Furthermore, nB_4C models with varying grain sizes from 4.07 nm to 10.86 nm display an inverse Hall–Petch relationship due to the GB sliding mechanism. A higher strain rate in nB_4C often leads to a higher yield strength, following a $2/3$ power relationship. These deformation mechanisms are critical for the design of ceramics with superior mechanical properties.

Keywords: nanocrystalline boron carbide, compression, grain boundary sliding, amorphization, inverse Hall–Petch behavior

PACS: 61.72.Mm, 62.20.F–, 02.70.Ns **DOI:** 10.1088/1674-1056/ad4989

1. Introduction

Nanocrystalline ceramics with nanosized grains often exhibit superior mechanical properties, such as high fracture toughness, high strength and super-plasticity in typically brittle behavior.[1–3] Extensive studies have explored the mechanical properties of nanocrystalline materials.[4–9] Generally, the mechanical behavior of nanocrystalline materials is strongly associated with grain boundary (GB) properties, such as grain size.[6,7,10–14] In nanocrystalline metals, the presence of GBs typically improves strength and ductility by blocking the movement of dislocations. This is described by the well-established Hall–Petch relationship, i.e., a reduction in grain size leads to an increase in yield strength.[10,15,16] However, when the mean grain size decreases below a critical threshold, the Hall–Petch relationship becomes ineffective due to diffusion-based mechanisms, such as GB sliding, GB diffusion and grain rotation.[17–19] It is believed that these diffusion-based mechanisms are easily activated compared with dislocation, contributing to the breakdown of Hall–Petch behavior.[20,21] In nanocrystalline ceramics, both Hall–Petch behavior and the inverse Hall–Petch effect have been observed,[11–13,22] but the underlying mechanisms remain unclear due to the limited dislocation activities in most ceramics under ambient conditions.

In most ceramics, amorphization is the main deformation mechanism for dissipating accumulated energy due to strong covalent bonding.[23–25] Generally, amorphization mechanisms are associated with crystal defects (dislocation, twinning and stacking faults),[23,26–28] structural transformation[29,30] and bond breakage.[27,31] In nanocrystalline ceramics, GBs play an important role in the deformation mechanisms due to the presence of disordered GB phases.[4–6,14,32] For example, amorphization in single-crystal 6H-SiC results from a structural transformation,[29] while nanocrystalline SiC under nanoindentation exhibits a crossover from continuous intergranular deformation to discrete intragranular deformation due to the interplay between cooperative grain motions and intergranular dislocation formation.[6] In single-crystal boron carbide (B_4C), amorphization mechanisms are mainly related to crystal defects,[23,26,27] destruction of the three-atom chain,[33–36] fracture of icosahedra[27,31] or transformation from $B_{11}C_p$(CBC) into B_{12}(CCC).[30] While in nanocrystalline B_4C (nB_4C), the results of shock simulation reveal three quasi-plastic deformation mechanisms: GB sliding, intergranular amorphization and intragranular amorphization.[5] Molecular dynamics (MD) simulations combined with experimental transmission electron microscopy suggest that GB sliding is the main deformation mechanism, leading to an inverse Hall–Petch relationship with mean grain sizes ranging from 4.84 nm to 14.64 nm, as well as intergranular amorphization.[14] Dislocation nucleation and glide in Al-doped B_4C lead to amorphization due to the breakage of weakened chain bonds.[37] However, nanocrystalline Al-doped B_4C displays a transition from the Hall–Petch to the inverse Hall–Petch relationship as the grain size decreases to its critical value of ~ 6 nm, determined by a competing mechanism between strengthening from shear homogenization and softening

[†]Corresponding author. E-mail: jun_li@whut.edu.cn
[‡]Corresponding author. E-mail: liulish@whut.edu.cn

© 2024 Chinese Physical Society and IOP Publishing Ltd

due to an increasing GB volume fraction.[11]

Furthermore, strain rate also plays an important role in the deformation behavior of materials.[38–45] For instance, MD simulations on hexagonal SiC under ramp dynamic loading with strain rates ranging from 10^8 s^{-1} to 10^{11} s^{-1} suggest that higher strain rates often lead to an increase in the strength, temperature and critical strain.[46] This effect is also observed in B_4C, where the uniaxial compressive strength increases with increasing strain rate,[42,44] following Kimberley's model.[47,48]

In particular, B_4C, as an advanced ceramic, draws particular attention for its potential technological applications in shielding and nuclear technology[49,50] due to its unique properties such as a high Hugoniot elastic limit (HEL) and low density.[49,51] However, under high-pressure conditions, B_4C often displays limited plasticity due to the formation of amorphous shear bands.[52,53] Although recent experiments and theoretical studies have been conducted to investigate the deformation mechanisms[4,5] and the Hall–Petch behaviors[4,11,14] in nB_4C, these behaviors under complex stress conditions remain unexplored due to the complicated crystal structure and bonding characteristics of B_4C.

Hence, we investigate the deformation mechanisms, the Hall–Petch behaviors with varying grain sizes from 4.04 nm to 10.86 nm and the strain-rate dependence of nB_4C under compression, using MD simulations with a machine-learning force field (ML-FF). The results reveal that the nB_4C model exhibits large quasi-plastic deformation, including GB sliding, intergranular amorphization and intragranular amorphization. The GB sliding arises from the pre-distorted icosahedra, facilitating intergranular amorphous band formation. Interaction between softened amorphous GBs and unfavorably oriented grains triggers destruction of the icosahedra within grains near GBs, resulting in the formation of intragranular amorphization and structural failure. Furthermore, the relationship between yield strength and grain size in nB_4C displays an inverse Hall–Petch effect due to the GB sliding mechanism. For strain-rate dependence, a higher strain rate leads to higher yield strength, following a $2/3$ power relationship.

2. Methods

We perform MD simulations to investigate the mechanical behavior of nB_4C under compression at room temperature. To carry out these simulations, we utilize the Large-scale Atomic/Molecular Massively Parallel Simulator (LAMMPS) software[54] and visualize the simulation results using the OVITO package.[55] The recently developed ML-FF[56] is employed to model the interatomic interaction of nB_4C, and demonstrates outstanding accuracy in describing the mechanical behaviors and amorphization of B_4C.[5,27,37,56] The ML-FF has been developed by training deep neural networks with data derived from density functional theory simulations. More details on the development and validation of the ML-FF can be found in our previous work.[5] In Ref. [5], the ML-FF exhibited good performance in describing the lattice constants, elastic properties, equation of state (EOS) and shock Hugoniot of B_4C, as well as the properties related to the GBs in MD simulations. This suggests that it is feasible for the ML-FF to be employed to investigate the behavior of nB_4C under high pressure in the present study.

Here, we focus on the most energetically favored configuration of $B_{11}C_p$(CBC),[30] which comprises 12-atom $B_{11}C_p$ icosahedral clusters connected by C–B–C three-atom chains.[49,51] The icosahedral clusters are located at the vertices of a rhombohedral lattice, while the three-atom chains align along [111] rhombohedral axis. Notably, in the present study, the three-index hexagonal notation is employed to denote the planes and directions.

To elucidate the mechanical behaviors and deformation mechanisms in nB_4C, we construct an nB_4C model using the Voronoi tessellation method,[57] denoted as GB1 and shown in Fig. 1. The GB1 model consists of 16 randomly oriented grains with dimensions of 16 nm×16 nm×80 nm, containing 2814985 atoms with a mean grain size of 10.86 nm. This model includes a total of 28 GBs. Generally, a small-angle GB is characterized by an orientation disparity between adjacent grains below 15°, while a large-angle GB surpasses this threshold.[58] Among these 28 GBs, 25 are classified as large-angle GBs. These large-angle GBs make up 89.3% of the total, consistent with the typical composition of the actual material in which the large-angle GBs usually represent the majority. Moreover, we also construct two other nB_4C models with grain sizes of 6.79 nm (GB2 model) and 4.07 nm (GB3 model) to investigate the Hall–Petch behaviors of nB_4C. To eliminate the influence of grain orientation, the grain orientations of GB1, GB2 and GB3 models are the same. The GB2 model contains 687269 atoms with dimensions of 10 nm×10 nm×50 nm, while the GB3 model comprises 148479 atoms with dimensions of 6 nm×6 nm×30 nm.

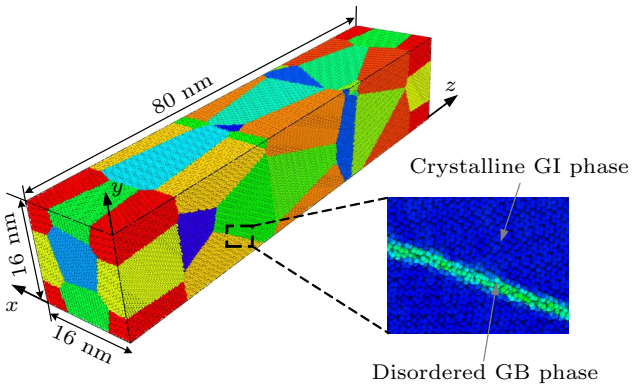


Fig. 1. The GB1 model with a mean grain size of 10.86 nm contains 16 randomly oriented grains with 2814985 atoms. The atoms are color-coded by the grain ID. GI stands for grain interior.

Before compression, thermal annealing is performed to relax the local internal stresses induced by the GBs. Each model is first annealed at 1000 K for 80 ps, then cooled down to 300 K for 20 ps using the NPT ensemble. Subsequently, the model is equilibrated at 300 K for 30 ps with the NVT ensemble. Finally, these equilibrium models are used to conduct compression simulations along the positive z-axis, using the NVE ensemble. This quasi-isentropic compression with increasing temperature is an adiabatic process under high pressure, demonstrating the dynamic behaviors of materials.[59,60] The value of strain rate for these simulations is set to 5×10^{9} s^{-1}, which is comparable to shock compression.[46] Furthermore, we employ the GB3 model to investigate the effects of strain rates, using a wide range of compressive strain rates ranging from 2×10^{9} s^{-1} to 1×10^{11} s^{-1}. Periodic boundary conditions are applied to eliminate the possible surface effects and the integration timestep is set to 1.0 fs.

To examine the mechanical behavior of nB_4C under compression, the physical properties of interest, such as stress (σ) and temperature (T), are analyzed. We quantify the stress components σ_{ij} (where i, $j = x$, y, z) by averaging over all the atoms, and per-atom stress is obtained by dividing its virial stress by the volume of the Voronoi cell around the atom. Thermodynamic variables and properties are calculated as follows:

$$P = \frac{1}{3}\left(\sigma_{xx}+\sigma_{yy}+\sigma_{zz}\right), \tag{1}$$

$$\tau = \frac{1}{2}\left[\sigma_{zz}-\frac{1}{2}\left(\sigma_{xx}+\sigma_{yy}\right)\right], \tag{2}$$

$$T = \frac{2}{3N}\frac{E_{\rm kin}}{k_{\rm B}}, \tag{3}$$

$$\sigma_{\rm vm} = \sqrt{\frac{1}{2}\left[(\sigma_{xx}-\sigma_{yy})^2+(\sigma_{yy}-\sigma_{zz})^2+(\sigma_{zz}-\sigma_{xx})^2+6(\sigma_{xy}^2+\sigma_{yz}^2+\sigma_{zx}^2)\right]}, \tag{4}$$

where P, τ and $\sigma_{\rm vm}$ are pressure, shear stress and von Mises stress, respectively. $E_{\rm kin}$ indicates the total kinetic energy, N stands for the total number of atoms and $k_{\rm B}$ is the Boltzmann constant.

The grain size has a great influence on the mechanical properties of nanocrystalline materials.[7,10,11,61–64] Generally, grain refinement enhances the strength of materials, as described by the well-established Hall–Petch relation, expressed as follows:

$$\sigma_{\rm s} = \sigma_0 + \frac{k}{\sqrt{d}}, \tag{5}$$

where $\sigma_{\rm s}$ is the yield strength and d is the grain size. σ_0 and k are material-dependent parameters.

Furthermore, to explore the effects of strain rates, the Kimberley model[47] is employed to describe the relationship between compressive strength $\sigma_{\rm c}$ and strain rate $\dot{\varepsilon}$ under dynamic compression. This Kimberley model is derived from fundamental physics governing crack initiation, growth and interaction, influenced by microstructural factors such as the defect size, as well as material parameters including Young's modulus (E) and fracture toughness ($K_{\rm IC}$).[47,48] The Kimberley model is defined as follows:

$$\sigma_{\rm c}/\sigma_0 = \left(\dot{\varepsilon}/\dot{\varepsilon}_0\right)^{2/3}+1, \tag{6}$$

$$\sigma_0 = \alpha\frac{K_{\rm IC}}{\bar{s}\eta^{1/4}}, \tag{7}$$

$$\dot{\varepsilon}_0 = \alpha\frac{v_{\rm c}K_{\rm IC}\eta^{1/4}}{\bar{s}E}, \tag{8}$$

where the parameters σ_0 and $\dot{\varepsilon}_0$ are the quasistatic compressive strength and the characteristic compressive strain rate, respectively. $\bar{s}$ is the average defect size, η represents the areal flaw density and $v_{\rm c}$ denotes the limiting crack growth speed. The term α is a dimensionless proportionality constant, ensuring the value of σ_0 is equal to the quasistatic compressive strength of a material described by parameters $\bar{s}$, η, E and $K_{\rm IC}$.

3. Results and discussion

3.1. Deformation mechanism of nB_4C

Generally, amorphization is the predominant deformation mechanism for the abnormal brittle failure of ceramics under pressure.[35,52] However, the GB1 model shows a relatively large quasi-plastic deformation (~ 0.1 strain) before mechanical failure. To understand this deformation mechanism in nB_4C, we plot the stress–strain curves and the strain-dependent average bond angle of chains and icosahedra for the GB1 model, as shown in Fig. 2. In addition, snapshots at critical strains identified by the von Mises shear strain are selected to illustrate the key events leading to the failure. For better clarity, we also analyze the temperature rise, as shown in Fig. 3(b). The stress–strain curve exhibits three distinct deformation regions: elastic deformation, quasi-plastic deformation and amorphization-induced failure. These regions are labeled as I, II and III, respectively, in Fig. 2(a).

Firstly, the uniformly elastic deformation from 0 to 0.075 strain occurs with a continuous increase in stress (Fig. 2(a)), displaying an almost constant temperature (Fig. 3(b)). Notably, the average angle of chains exhibits a sudden reduction (Fig. 2(b)) at ~ 0.05 strain due to the interaction of chains and icosahedra. Moreover, no significant structural changes are observed, as shown in Fig. 2(c). Subsequently,

the quasi-plastic deformation from 0.076 to 0.164 is characterized by a significant increase in temperature (Fig. 3(b)). Indeed, the model experiences GB sliding (Fig. 2(d)), subsequent intergranular amorphization (Fig. 2(e)) and final intragranular amorphization (Fig. 2(e)). In addition, the angle of the chains displays a significant reduction during quasi-plastic deformation (Fig. 2(b)), suggesting that more chains continue to bend. Finally, mechanical failure beyond 0.164 strain arises from intragranular amorphous band formation, leading to a decrease in the stress (Fig. 2(f)) and complete structural failure (Fig. 2(g)). The maximum values of von Mises stress and shear stress are 31.7 GPa and 15.8 GPa at 0.164 strain. Unlike single-crystal B_4C, where the stress decreases suddenly upon reaching its peak value,[27,65] the nB_4C model decreases gradually with a slight slope over a narrow strain range (Fig. 2(a)). Notably, various grains within the GB1 model experience different deformations due to the highly anisotropic nature of B_4C.[52,66,67] To eliminate the special features induced by an individual case, we construct four nB_4C models with different grain orientations, as shown in Fig. S1(a) in the supplementary material. For computational efficiency, each model has dimensions of 6 nm×6 nm×30 nm. Quasi-isentropic compressions are performed on these four models at a strain rate of 5×10^9 s^{-1}. The structures at strain 0.320 are shown in Fig. S1(b), and exhibit similar behavior in which grains with unfavorable orientations may undergo intragranular amorphization while other grains may experience intergranular amorphization. These results reveal that the deformation mechanisms of nB_4C are independent of the distribution of grain orientations.

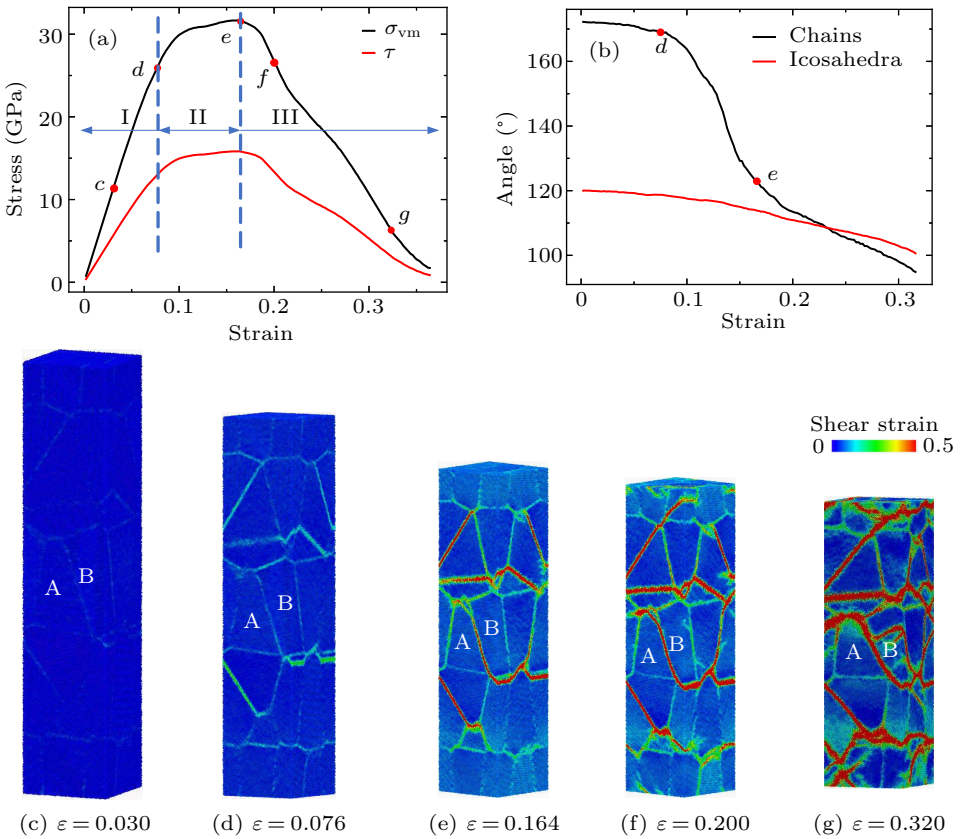


Fig. 2. The compression behavior and failure process of the GB1 model. (a) The stress–strain relationship. I, II and III represent elastic deformation, quasi-plastic deformation and failure, respectively. (b) The average angle of three-atom chains and intra-icosahedra change with strain. (c) The structure at the compression strain $\varepsilon = 0.030$, which remains relatively unchanged. (d) The structure at $\varepsilon = 0.076$, where quasi-plastic deformation initiates. (e) The structure at $\varepsilon = 0.164$, where the von Mises stress reaches its maximum value. (f) The structure at $\varepsilon = 0.200$. (g) The structure at $\varepsilon = 0.320$ is completely damaged. A and B denote the two grains presented in Figs. 4 and 5.

To investigate the phase transformations, we also examine the EOS for the GB1 model, including pressure–volume (P–V) and temperature–pressure (T–P) relationships under pressure, as shown in Fig. 3. The regions of elastic deformation (region I), quasi-plastic deformation (region II) and failure (region III) are identified in Fig. 3. The EOS of materials at extreme pressures can be described by the Murnaghan EOS function,[68] expressed as follows:

$$P(V) = \frac{K}{K'}\left[\left(\frac{V}{V_0}\right)^{-K'} - 1\right], \tag{9}$$

where P represents the pressure and V_0 and V are the initial volume and deformed volume, respectively. K and K', as fitting parameters, denote the bulk modulus and the first derivative of the bulk modulus with respect to pressure, respectively.

The P–V relationship, as shown in Fig. 3(a), follows the Murnaghan EOS function, in good agreement with the results of first-principles simulations[35] and shock data.[5,69] Nevertheless, the regions associated with phase transformations show a deviation from the Murnaghan EOS fitting. This deviation for the GB1 model occurs at a pressure of 16.9 GPa, as indicated in Fig. 3, agreeing well with the HEL (15–20 GPa). Structural failure appears at a pressure of 42.4 GPa (Fig. 3). In addition, the parameter K calculated from the model is 246 GPa, consistent with the value of QM simulations under hydrostatic compression (240 GPa),[5] as well as the experimental value (237 GPa).[70] However, the value obtained for the parameter K' is 1.13, which is much lower than the value of 3.2 under hydrostatic compression.[5] This discrepancy may be mainly associated with the absence of phase transformation during hydrostatic compression, which significantly affects the properties of materials. Furthermore, as shown in Fig. 3(b), the temperature rises in the T–P curve for the GB1 model is much lower than the shock compression data.[71,72] This behavior is similar to the temperature–volumetric–strain relationship observed in the SiC ceramic under quasi-isentropic compression.[46,59]

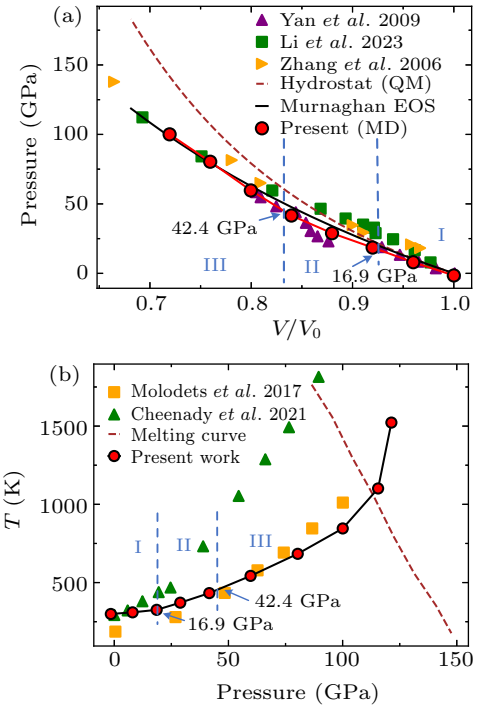


Fig. 3. Equation of state (EOS) for the GB1 model. (a) Pressure–volume data from our simulations and the Murnaghan EOS function. (b) Temperature–pressure relationship compared with the results of previous studies. I, II and III represent the elastic deformation, quasi-plastic deformation and failure, respectively.

To elucidate the underlying mechanism of quasi-plastic deformation in the GB1 model, we examine the local structural evolution at critical strains, as shown in Fig. 4. Furthermore, we investigate the stress state of the local structures to reveal the stress distribution of nB_4C, as illustrated in Fig. 5. This local structure involves two grains: grain A and grain B, marked in Fig. 2. The orientations of grain A and grain B are listed in Table 1. The orientation difference between the two grains is 72.3°. Initially, the dominant quasi-plastic deformation mechanism is GB sliding, characterized by the most slipped icosahedra being along GBs (Fig. 4(b)) due to the presence of pre-distorted icosahedra within the GBs (Fig. 4(a)). Meanwhile, the chains within both grain A and grain B are almost straight and suffer higher axial stress (Fig. 5(a)). Subsequently, GB sliding facilitates intergranular amorphous band formation as the stress increases (Fig. 4(c)). Notably, the chains in grain A experience bending due to interactions with adjacent icosahedra. The bending chains may further result in the formation of new covalent bonds between chains and neighboring icosahedra, increasing stress within the icosahedra (Fig. 5(b)). Hence, the interplay between the softening amorphous GBs and these icosahedra with increased stress in grain A triggers the deconstruction of icosahedra within the grain, leading to intragranular amorphization (Fig. 4(d)). For instance, when the strain reaches 0.124, intergranular amorphization is observed to propagate towards internal grain A, indicating the initiation of intragranular amorphization. At 0.150 strain, intragranular amorphous bands are formed (Fig. 5(c)). Despite the formation of intragranular amorphization in grain A, the structure in grain B remains almost unchanged (Fig. 5(c)), indicating its ability to resist compressive loading. This behavior suggests that intragranular amorphization preferentially occurs in grains with unfavorable orientations, while other grains with more favorable orientations undergo distortion without icosahedral deconstruction.

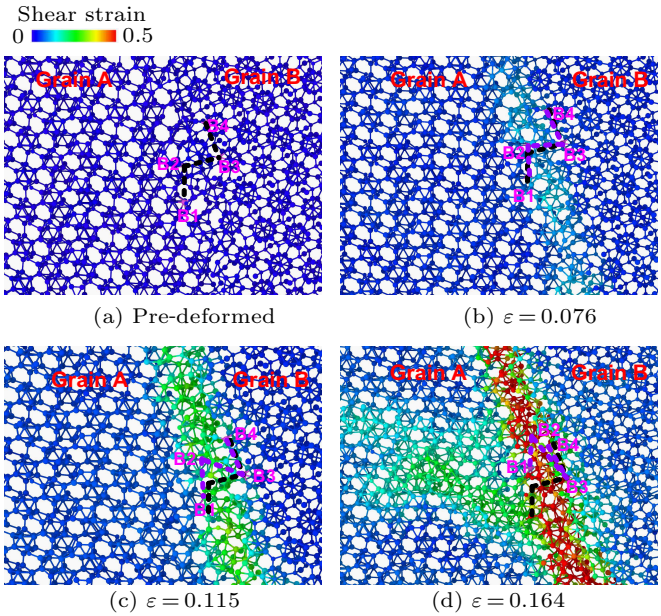


Fig. 4. The local structural evolution with structures including grain A and grain B, colored by the von Mises shear strain map at various strains. (a) The structure before the structural change. (b) The structure at 0.076 strain where GB sliding occurs. (c) The structure at 0.115 strain where intergranular amorphization occurs. (d) The structure at 0.164 where intragranular amorphization forms in grain A. The magenta balls represent the atoms B1–B4 in different icosahedra near the GB.

Table 1. The orientations of grain A and grain B.

Grain	Grain ID	*x*-axis	*y*-axis	*z*-axis
A	10	$[\bar{1}031]$	$[\bar{8}\,\bar{1}77]$	[351]
B	14	$[125\bar{1}]$	$[011\bar{1}]$	[10 13 18]

Finally, at 0.164 strain, intragranular amorphous bands form and develop (Fig. 4(d)), resulting in mechanical failure. The intragranular amorphous band in grain A aligns with a slip system of $(1\bar{2}1)/[012]$. Meanwhile, grain A experiences significant sliding and rotation, as illustrated by the black dashed lines connecting atoms B1–B4 in an initial structure compared with the purple dashed lines in a deformed structure (Fig. 4(d)). Notably, the stress may reach the maximum value, following increased stress within icosahedra in all grains due to the formation of new B–B bonds between chains and neighboring icosahedra (Fig. 5(d)). Overall, GB sliding is the main quasi-plastic deformation mechanism in nB_4C due to the presence of the pre-distorted icosahedra within GBs. Intergranular amorphization mainly arises from GB sliding, while intragranular amorphization results from the interplay between the softening amorphous GBs and grains with unfavorable orientations.

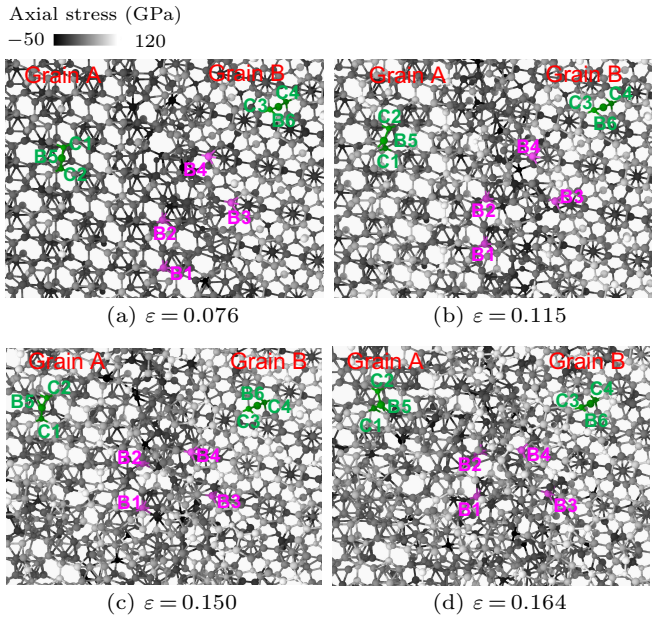


Fig. 5. The local structural evolution within the GB involving grain A and grain B, with structures colored by the axial stress map in white and black. (a) The structure at 0.076 strain, where the chains suffer greater stress in both grain A and grain B. (b) The structure at 0.115 strain, where the chains in grain A form new B–B bonds with neighboring icosahedra. (c) The structure at 0.150, where intragranular amorphization has formed in grain A. (d) The structure at 0.164, where the chains in grain B form new B–B bonds with neighboring icosahedra. The magenta balls represent the atoms B1–B4 in different icosahedra near the GB, and the green balls mark the C1–B5–C2, C3–B6–C4 chains.

Structural analyses along the MD trajectory indicate that the formation of amorphization is related to the rearrangement of chemical bonds around the icosahedra. The radial distribution function (RDF) of the initial and deformed structure is used to quantify the extent of local amorphization in nB_4C, as shown in Fig. 6. The bonds in B_4C can be categorized into four types: intra-chain, chain–icosahedra, inter-icosahedra and intra-icosahedra. The bond lengths for these bond types in the initial B_4C structure are ~ 1.433 Å, ~ 1.608 Å, ~ 1.716 Å and ~ 1.759–1.805 Å, respectively.[73,74] The RDF peaks of the initial B_4C structure can be identified based on these bond lengths, as shown in (Fig. 6(a)). The RDF peaks at relatively large distances (≥ 3.5 Å) are used to identify the long-range crystalline order.[72] First, the RDF of the initial nB_4C structure is compared with that of single-crystal B_4C (Fig. 6(a)). This suggests that the RDF peaks for the intra-chain, chain–icosahedral, inter- and intra-icosahedra bonds in the nB_4C and single-crystal B_4C structures nearly overlap, while those for the long-range crystalline order in nB_4C decrease due to the presence of disordered GB phases.

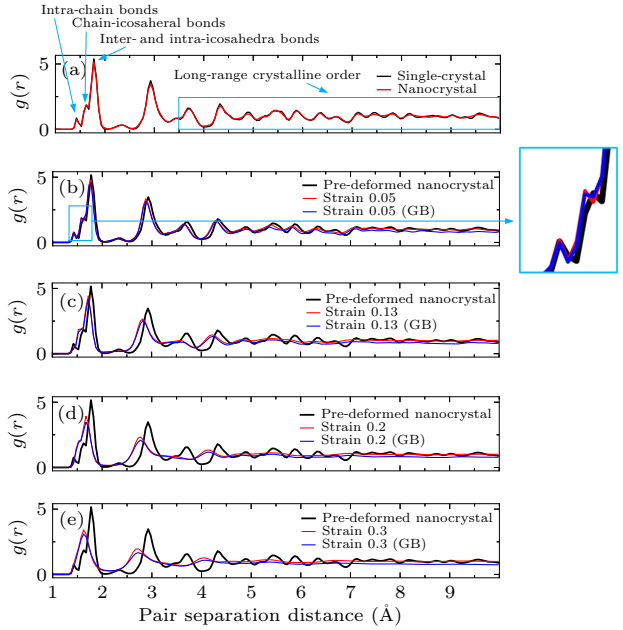


Fig. 6. The radial distribution function of the initial and deformed nB_4C at various strains.

To exhibit the GB contributions, we examined the RDF of the GB between grain A and grain B in Fig. 6. At a low strain of 0.05, the RDF peaks for intra-chain and chain–icosahedral bonds in the nB_4C model remain almost unchanged, while the RDF peak for chain–icosahedral bonds in the GB model decreases (Fig. 6(b)). In addition, the RDF peak for inter- and intra-icosahedral bonds in the GB model exhibits a more significant reduction compared with the nB_4C model, indicating more pronounced deformation within the GB. This suggests that the elastic deformation primarily involves icosahedral compression, highlighting the higher intrinsic strengths of intra-chain and chain–icosahedral bonds compared with inter- and intra-icosahedral bonds in B_4C. As strain increases, the RDF peaks for intra-chain, chain–icosahedral and inter- and intra-icosahedral bonds further decrease, while the RDF peaks for long-range order are gradually lost (Figs. 6(c)–6(e)). This mainly arises from the formation of localized amorphization. In particular, the GBs of nB_4C become more disordered.

3.2. The effect of grain size in nB_4C

To investigate the effect of grain size on nB_4C, we examine the deformation behaviors of three nB_4C models with mean grain sizes of 10.86 nm, 6.79 nm and 4.07 nm for models GB1, GB2 and GB3, respectively. The compression behavior of nB_4C for the three models is shown in Fig. 7. The maximum von Mises stresses are 31.7 GPa at 0.164 strain for GB1, 29.7 GPa at 0.120 strain for GB2 and 27.0 GPa at 0.135 strain for GB3, as illustrated in Fig. 7(a). The yield strength increases with increasing grain size, following the inverse Hall–Petch relationship (Fig. 7(b)), expressed as $\sigma_s = 39.1 - 24.4/\sqrt{d}$. This inverse Hall–Petch behavior mainly arises from GB sliding. As the grain size decreases, the volume fraction of soft GBs increases, leading to easier activation of GB sliding. This is consistent with the GB sliding inducing the inverse Hall–Petch behavior of nB_4C under shear deformation.[14] These yield strengths in nB_4C are much lower than for single-crystal B_4C (58.6 GPa), indicating that the presence of GBs reduces the strength of B_4C.

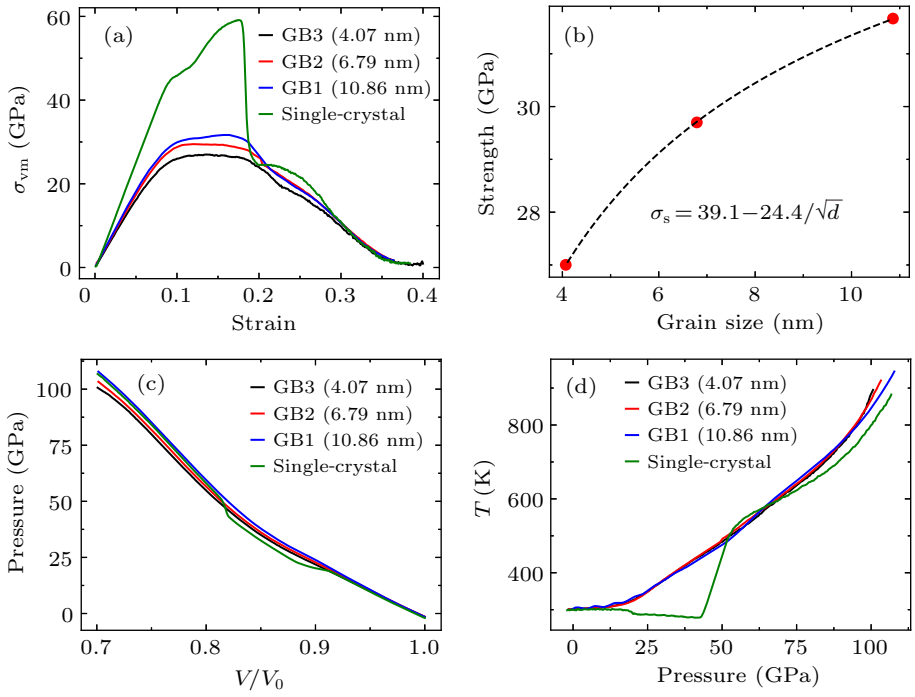


Fig. 7. The compression behavior for three nB_4C models. (a) Stress–strain relationships. (b) The Hall–Petch behavior. (c) *P*–*V* relationship for nB_4C and single-crystal B_4C. (d) *T*–*P* relationship for nB_4C and single-crystal B_4C.

In addition, in Fig. 7(c) for the *P*–*V* relationship and Fig. 7(d) for the *T*–*P* relationship, the three nB_4C models display a continuous increase in pressure and temperature while the single-crystal B_4C model exhibits a sudden change. This may be attributed to the influence of GBs on the properties of ceramics. The quasi-plastic deformation is characterized by temperature rise at a pressure of 16.9 GPa for GB1, 15.4 GPa for GB2 and 15.0 GPa for GB3, as shown in Fig. 7(d). These values are lower than the value in single-crystal B_4C (18.7 GPa), consistent with the HEL (15–20 GPa).

3.3. The effect of strain rate in nB_4C

Experiments have revealed that the strain rate has a great influence on the yield strength of materials.[39,48] Here, we employ the GB3 model to explore the effect of strain rate on nB_4C, with a wide range of compressive strain rates ranging from 2×10^9 s^{-1} to 1×10^{11} s^{-1}, as shown in Fig. 8.

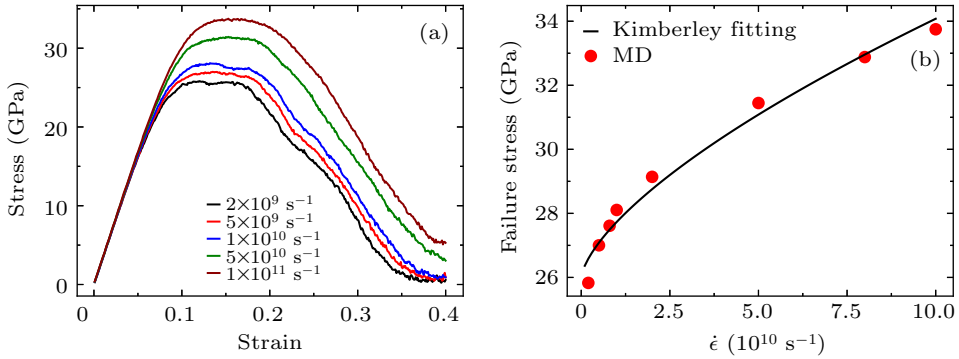


Fig. 8. Strain rate dependence of nB_4C. (a) Von Mises stress versus strain. (b) Compressive strength versus strain rate.

The strengths are 25.8 GPa at 0.120 strain, 27.0 GPa at 0.135 strain, 28.1 GPa at 0.132 strain, 31.4 GPa at 0.153 strain and 33.7 at 0.153 strain for strain rates of 2×10^{9} s^{-1}, 5×10^{9} s^{-1}, 1×10^{10} s^{-1}, 5×10^{10} s^{-1} and 1×10^{11} s^{-1}, respectively. A higher strain rate leads to higher strength (Fig. 8(a)), consistent with experimental observations.[39,48] Furthermore, as shown in Fig. 8(b), the relationship between the strength and strain rate of nB_4C follows a $2/3$ power law, in good agreement with the Kimberley model.[48]

4. Conclusion

In summary, we construct three nB_4C models with different grain sizes (ranging from 4.07 nm to 10.86 nm) to investigate the compression behavior, quasi-plastic deformation mechanism, Hall–Petch behavior and strain rate effect of nB_4C, using MD simulations with ML-FF. Our major findings are as follows.

The presence of the GB reduces the yield strength compared with single-crystal B_4C, leading to a relatively large quasi-plastic deformation in nB_4C. The quasi-plastic deformation involves GB sliding, intergranular amorphization and intragranular amorphization.

GB sliding results from the soft GBs, contributing to intergranular amorphization. Intragranular amorphization arises from the interplay between the softening amorphous GBs and grains with unfavorable orientations, resulting in structural failure.

The relationship between yield strength and grain size for nB_4C displays an inverse Hall–Petch behavior due to the GB sliding mechanism.

A higher strain rate corresponds to a higher yield strength, following a $2/3$ power relationship.

This study elucidates the deformation behaviors in nB_4C, providing a new way to design ceramics with excellent performance.

Data availability statement

The datasets generated during and/or analyzed during the current study are available from the corresponding author on reasonable request.

Acknowledgement

The authors acknowledge the support from the National Natural Science Foundation of China (Grant No. 11972267).

References

[1] Xu H, Ji W, Jiang J, Liu J, Wang H, Zhang F, Yu R, Tu B, Zhang J, Zou J, Wang W, Wu J and Fu Z 2023 *Nat. Commun.* **14** 4889
[2] Madhav Reddy K, Guo J J, Shinoda Y, Fujita T, Hirata A, Singh J P, McCauley J W and Chen M W 2012 *Nat. Commun.* **3** 1052
[3] Zhang S, Sun D, Fu Y and Du H 2003 *Surf. Coatings Technol.* **167** 113
[4] Guo D and An Q 2019 *Int. J. Plast.* **121** 218
[5] Li J and An Q 2023 *J. Eur. Ceram. Soc.* **43** 208
[6] Szlufarska I, Nakano A and Vashishta P 2005 *Science* **309** 911
[7] Ryou H, Drazin J W, Wahl K J, Qadri S B, Gorzkowski E P, Feigelson B N and Wollmershauser J A 2018 *ACS Nano* **12** 3083
[8] Messing G L and Stevenson A J 2008 *Science* **322** 383
[9] Shao Y F, Yang X, Zhao X and Wang S Q 2012 *Chin. Phys. B* **21** 083101
[10] Hansen N 2004 *Scr. Mater.* **51** 801
[11] Li J, Luo K and An Q 2023 *J. Eur. Ceram. Soc.* **44** 659
[12] Li W, Hahn E N, Yao X, Germann T C, Feng B and Zhang X 2020 *Acta Mater.* **200** 632
[13] Maita J M, Rommel S, Davis J R, Ryou H, Wollmershauser J A, Gorzkowski E P, Feigelson B N, Aindow M and Lee S W 2023 *Acta Mater.* **251** 118881
[14] Guo D, Song S, Luo R, Goddard W A, Chen M, Reddy K M and An Q 2018 *Phys. Rev. Lett.* **121** 145504
[15] Han Q and Yi X 2022 *Int. J. Plast.* **153** 103261
[16] Sansoz F and Ke X 2022 *Acta Mater.* **225** 117560
[17] Han Q and Yi X 2021 *J. Mech. Phys. Solids.* **154** 104530
[18] Duan F H, Naunheim Y, Schuh C A and Li Y 2021 *Acta Mater.* **213** 116950
[19] Chandiran E, Ogawa Y, Ueji R and Somekawa H 2023 *J. Alloys Compd.* **930** 167443
[20] Van Swygenhoven H 2002 *Science.* **296** 66
[21] Hasnaoui A, Derlet P M and Van Swygenhoven H 2004 *Acta Mater.* **52** 2251
[22] Wollmershauser J A, Feigelson B N, Gorzkowski E P, Ellis C T, Goswami R, Qadri S B, Tischler J G, Kub F J and Everett R K 2014 *Acta Mater.* **69** 9
[23] Zhao S, Kad B, Remington B A, Lasalvia J C, Wehrenberg C E, Behler K D and Meyers M A 2016 *Proc. Natl. Acad. Sci. USA* **113** 12088
[24] Zhao S, Li B, Remington B A, Wehrenberg C E, Park H S, Hahn E N and Meyers M A 2021 *Mater. Today.* **49** 59
[25] Zhao S, Flanagan R, Hahn E N, Kad B, Remington B A, Wehrenberg C E, Cauble R, More K and Meyers M A 2018 *Acta Mater.* **158** 206
[26] Reddy K M, Guo D, Song S, Cheng C, Han J, Wang X, An Q and Chen M 2021 *Sci. Adv.* **7** eabc6714
[27] Shen Y, Reddy K M, Li J, Chen M and An Q 2023 *Acta Mater.* **249** 118828
[28] Jiang C, Zheng M J, Morgan D and Szlufarska I 2013 *Phys. Rev. Lett.* **111** 155501
[29] Wu Z, Liu W, Zhang L and Lim S 2020 *Acta Mater.* **182** 60
[30] Fanchini G, McCauley J W and Chhowalla M 2006 *Phys. Rev. Lett.* **97** 035502
[31] An Q and Goddard W A 2015 *Phys. Rev. Lett.* **115** 105501
[32] Luo J 2023 *Interdiscip. Mater.* **2** 137
[33] Aryal S, Rulis P and Ching W Y 2011 *Phys. Rev. B* **84** 184112
[34] Taylor D C E 2015 *J. Am. Ceram. Soc.* **98** 3308
[35] Yan X Q, Tang Z, Zhang L, Guo J J, Jin C Q, Zhang Y, Goto T, McCauley J W and Chen M W 2009 *Phys. Rev. Lett.* **102** 075505
[36] Meille S, Lombardi M, Chevalier J and Montanaro L 2016 *Comput. Mater. Sci.* **121** 106
[37] Li J, Luo K and An Q 2023 *Phys. Rev. Lett.* **130** 116104
[38] Hu G, Ramesh K T, Cao B and McCauley J W 2011 *J. Mech. Phys. Solids.* **59** 1076
[39] Nemat-Nasser S and Deng H 1994 *Acta Metall. Mater.* **42** 1013
[40] Zheng J, Ji M, Zaiemyekeh Z, Li H and Hogan J D 2022 *J. Eur. Ceram. Soc.* **42** 7516
[41] Paliwal B and Ramesh K T 2007 *Scr. Mater.* **57** 481
[42] Ghosh D, Subhash G, Zheng J Q and Halls V 2012 *J. Appl. Phys.* **111** 063523
[43] Pittari J, Subhash G, Zheng J, Halls V and Jannotti P 2015 *J. Eur. Ceram. Soc.* **35** 4411
[44] Venkatesan J, Iqbal M A and Madhu V 2020 *Thin-Walled Struct.* **154** 106785
[45] Hogan J D, Farbaniec L, Shaeffer M and Ramesh K T 2015 *J. Am. Ceram. Soc.* **98** 902
[46] Feng L, Li W, Hahn E N, Branicio P S, Zhang X and Yao X 2022 *Mech. Mater.* **164** 104139
[47] Hogan J D, Farbaniec L, Sano T, Shaeffer M and Ramesh K T 2016 *Acta Mater.* **102** 263
[48] Kimberley J, Ramesh K T and Daphalapurkar N P 2013 *Acta Mater.* **61** 3509

[49] Domnich V, Reynaud S, Haber R A and Chhowalla M 2011 *J. Am. Ceram. Soc.* **94** 3605
[50] Awasthi A and Subhash G 2020 *Prog. Mater. Sci.* **112** 100664
[51] Thévenot F 1990 *J. Eur. Ceram. Soc.* **6** 205
[52] Chen M, McCauley J W and Hemker K J 2003 *Science* **299** 1563
[53] Reddy K M, Liu P, Hirata A, Fujita T and Chen M W 2013 *Nat. Commun.* **4** 2483
[54] Plimpton S 1995 *J. Comput. Phys.* **117** 1
[55] Stukowski A 2010 *Model. Simul. Mater. Sci. Eng.* **18** 015012
[56] An Q 2021 *Phys. Rev. Mater.* **5** 103602
[57] Frøseth A G, Van Swygenhoven H and Derlet P M 2005 *Acta Mater.* **53** 4847
[58] Winning M and Rollett A D 2005 *Acta Mater.* **53** 2901
[59] Li W, Hahn E N, Branicio P S, Yao X, Zhang X, Feng B and Germann T C 2021 *Int. J. Plast.* **138** 102923
[60] Zhu Q, Shao J L and Wang P 2023 *J. Nucl. Mater.* **574** 154200
[61] Zare Chavoshi S, Branicio P S and An Q 2021 *Phys. Rev. Mater.* **5** 073606
[62] Figueiredo R B and Langdon T G 2021 *J. Mater. Res. Technol.* **14** 137
[63] Meyers M A, Vöhringer O and Lubarda V A 2001 *Acta Mater.* **49** 4025
[64] Yu H, Xin Y, Wang M and Liu Q 2018 *J. Mater. Sci. Technol.* **34** 248
[65] Li X, Liu L, Mei H, Xu S, Li J and Zhang J 2021 *Comput. Mater. Sci.* **199** 110708
[66] Chauhan A, Schaefer M C, Haber R A and Hemker K J 2019 *Acta Mater.* **181** 207
[67] Li J, Xu S, Zhang J Y, Liu L S, Liu Q W, She W C and Fu Z Y 2017 *Chin. Phys. B* **26** 047101
[68] Murnaghan F D 1944 *Proc. Natl. Acad. Sci. USA* **30** 244
[69] Zhang Y, Mashimo T, Uemura Y, Uchino M, Kodama M, Shibata K, Fukuoka K, Kikuchi M, Kobayashi T and Sekine T 2006 *J. Appl. Phys.* **100** 113536
[70] Mcclellan K J, Chu F, Roper J M and Shindo I 2001 *J. Mater. Sci.* **36** 3403
[71] Molodets A M, Golyshev A A and Shakhrai D V. 2017 *J. Exp. Theor. Phys.* **124** 469
[72] Cheenady A A, Awasthi A, Devries M, Haines C and Subhash G 2021 *Phys. Rev. B* **104** 184110
[73] Cheng C, Reddy K M, Hirata A, Fujita T and Chen M 2017 *J. Eur. Ceram. Soc.* **37** 4514
[74] Aselage T L, Van Deusen S B and Morosin B 1990 *J. Less-Common Met.* **166** 29